Navier–Stokes and Potential Calculations of Axial Spacing Effect on Vortical and Potential Disturbances and Gust Response in an Axial Compressor

M.-H. Chung

A. M. Wo

Institute of Applied Mechanics,
National Taiwan University,
Taipei 106, Taiwan

The effect of blade row axial spacing on vortical and potential disturbances and gust response is studied for a compressor stator/rotor configuration near design and at high loadings using two-dimensional incompressible Navier–Stokes and potential codes, both written for multistage calculations. First, vortical and potential disturbances downstream of the isolated stator in the moving frame are defined; these disturbances exclude blade row interaction effects. Then, vortical and potential disturbances for the stator/rotor configuration are calculated for axial gaps of 10, 20, and 30 percent chord. Results show that the potential disturbance is uncoupled locally; the potential disturbance calculated from the isolated stator configuration is a good approximation for that from the stator/rotor configuration upstream of the rotor leading edge at the locations studied. The vortical disturbance depends strongly on blade row interactions. Low-order modes of vortical disturbance are of substantial magnitude and decay much more slowly downstream than do those of potential disturbance. Vortical disturbance decays linearly with increasing mode except very close to the stator trailing edge. For a small axial gap, e.g., 10 percent chord, both vortical and potential disturbances must be included to determine the rotor gust response.

1.0 Introduction

An understanding of blade unsteady force is vital for design considerations of structural integrity in turbomachines. This unsteady loading is due to two effects: response to flow unsteadiness on a rigid blade and vibratory blade motion. In general, the flow unsteadiness, acting as a forcing function, includes wakes and the potential field from the upstream blade row, the potential effect from the downstream row, and all other time-varying flow features. Disastrous blade failure can occur when the flow excitation frequency matches the blade natural frequency. Thus, a sound understanding of the sources of unsteadiness is vital for prediction of unsteady blade force.

Many researchers have undertaken the study of gust and gust response in axial compressors. Since an exhaustive list of excellent contributions is not feasible here, the reader is referred to AGARD (1987) for reference. Kielb and Chiang (1992) provided a summary of recent advances in forced response analyses. Verdon (1993) reviewed unsteady aerodynamic methods for turbomachinery aeroleastic and aeroacoustic applications.

As the axial space between blade rows is decreased, blade row flow interaction increases. Aerodynamically, limited data seem to suggest a beneficial effect, but the underlying physics is unclear. Smith (1969) reported an increase in the peak static pressure rise by about 6 percent and design efficiency of 1 percent in a four-stage compressor with a blade average axial gap decrease from 36.5 to 7.0 percent chord. Mikolajczak (1976) confirmed this view by showing data with an increase in peak isentropic enthalpy rise of 4 percent and design adiabatic efficiency of about 1 percent when axial spacing is decreased. However, Hetherington and Moritz (1976) argued that blade rows should be separated sufficiently so that most of the wake mixing can occur between rows. Aeromechanically, the present understanding of axial gap effect also needs clarification. Among others, Fleeter et al. (1981) carried out an important experimental study on the effect of axial spacing on gust response for a rotor/stator configuration and reported that the unsteady blade surface pressure increases significantly with decreased spacing at 100 percent speed but not at 70 percent speed. They also observed wave-related phenomenon from unsteady pressure data. Gallus et al. (1982) undertook extensive investigation of the blade number ratio and blade row spacing on stator dynamic loading and stage sound pressure level. They found that both vortical and potential effects are important in determining the blade response for very small gap. Recently, Manwaring and Wisler (1993) made a substantial contribution in comparing current state of the art gust response analyses with experimental data. They showed that an approach in which the unsteady gust is linearized about the time mean nonlinear flow is appropriate. Among other conclusions, they highlighted the importance of properly accounting for both vortical and potential disturbances in predicting gust response.

2.0 Objectives and Approach

The goal of this paper is to examine effects of axial spacing on vortical and potential disturbances and rotor gust response. We seek to answer, in part, the following questions:

- How large are the vortical and potential disturbances for various axial gaps and time-mean loadings?
- How does the axial gap affect rotor gust response?

Both Navier–Stokes and potential codes are used to address these questions for a stator/rotor configuration with axial gaps

Contributed by the International Gas Turbine Institute and presented at the 40th International Gas Turbine and Aeroengine Congress and Exhibition, Houston, Texas, June 5–8, 1995. Manuscript received by the International Gas Turbine Institute March 10, 1995. Paper No. 95-GT-301. Associate Technical Editor: C. J. Russo.

of 10, 20, and 30 percent chord and at two loadings. The approach taken is as follows. First, Navier–Stokes and potential calculations for an isolated stator are performed to determine vortical and potential disturbances as seen in the moving frame. This also serves to define disturbances without the presence of the rotor, thus without blade row interaction effects. Then, calculations are done for a stator/rotor configuration at all three axial gaps and two loadings. Flow variables in the gap region are presented. Vortical and potential disturbances are computed in the rotor frame at a *fixed* axial distance upstream of the rotor, along the extension of its camber line at the leading edge. This allows comparison of disturbances for different axial spacings on an equal basis. Finally, the amplitude and phase of unsteady rotor surface pressure are presented and discussed.

3.0 Navier–Stokes Calculation

This calculation is largely based on the work of Patankar and Spalding (1972). The following briefly describes the code. The unsteady flow in the blade passage is governed by the transformed incompressible continuity equation:

$$\nabla \cdot \mathbf{u} = 0 \tag{1}$$

with a reference frame attached to either stator or rotor. The form of the Reynolds-averaged Navier–Stokes equation used is:

$$\frac{\partial \mathbf{u}}{\partial t} + \nabla \cdot [(\mathbf{u} - \mathbf{u}_b)\mathbf{u}] = -\nabla P + \nabla \cdot [(\mu + \mu_t)\nabla \mathbf{u}]. \tag{2}$$

The modified Launder–Sharma (LS) low-Re version of $k-\epsilon$ two-equation model (Morse, 1991) is used to close these equations via the eddy viscosity coefficient μ_t. The equations governing these two variables are:

$$\frac{\partial k}{\partial t} + \nabla \cdot \; [(u - u_b)k] = \nabla \cdot \left[\left(\mu + \frac{u_t}{\sigma_k} \nabla k \right) \right] + G_k - \epsilon - D \tag{3}$$

$$\frac{\partial \epsilon}{\partial t} + \nabla \cdot [(u - u_b)\epsilon] = \nabla \cdot \left[\left(\mu + \frac{\mu_t}{\sigma_\epsilon} \right) \nabla \epsilon \right] + C_1 f_{\mu_1} G_k \frac{\epsilon}{k} - C_2 f_{\mu_2} \frac{\epsilon^2}{k} + E - F \tag{4}$$

where $G_k = \mu_t \, (\partial u_i / \partial x_k) \, (\partial u_i / \partial x_k + \partial u_k / \partial x_i)$, $D = 2\mu(\partial \sqrt{k} / \partial x_j)^2$, $E = 2\mu\mu_t(\partial^2 u_i / \partial x_j^2)$, $F = 2\mu(\partial \sqrt{\epsilon} / \partial x_j)^2$, $C_\mu = 0.09$, $C_1 = 1.44$, $C_2 = 1.92$, $\sigma_\kappa = 1$, $\sigma_\epsilon = 1.22$, $f_\mu = [1 - \exp(-y^+ / A^+)]^2$, $A^+ = 25$, $f_{\mu_1} = 1$ and $f_{\mu_2} = 1 - .21875 \exp(-R_t^2/36)$ with the eddy viscosity coefficient $\mu_t \equiv$

Nomenclature

A = coefficient of harmonic potential disturbance
C = chord
C_p = static pressure coefficient
D = coefficient of harmonic vortical disturbance
h_k = k^{th} data in a series analyzed by FFT
H_n = amplitude of the n^{th} harmonic from FFT
$\mathbf{i}/\mathbf{j}$ = unit vector in the axial/circumferential direction
L = 2π/disturbance pitch
M = Mach number
p = static pressure
$\hat{p}_i^+$ = i^{th} harmonic static pressure
Re = Reynolds number based on inlet flow velocity and blade chord
R_t = turbulence Re
S = circumferential blade pitch
s = solidity
T = rotor blade passing period
Tu = turbulence intensity
t = time
U_∞ = inlet uniform velocity
u^+ = streamwise component of periodic unsteady velocity
u_{NS}^+ = streamwise component of periodic unsteady velocity from *NS* code
u_p^+ = streamwise component of periodic unsteady velocity from potential code
u_v^+ = vortical part of streamwise component of periodic unsteady velocity
$\hat{u}_i^+$ = i^{th} harmonic streamwise gust
$|\hat{u}_i^+|$ = amplitude of the i^{th} harmonic streamwise gust
$\mathbf{u} = u\mathbf{i} + v\mathbf{j}$ = absolute flow velocity vector
$\mathbf{u}_b$ = rotor blade wheel velocity vector
V = periodic unsteady absolute velocity
V_b = rotor blade wheel speed
V_e = velocity outside the war layer in the far wake test case (see caption of Fig. 5)
$\bar{V}_z$ = axial component of time-mean velocity
v^+ = transverse component of periodic unsteady velocity
v_{NS}^+ = transverse component of periodic unsteady velocity from *NS* code
v_p^+ = transverse component of periodic unsteady velocity from potential code
v_v^+ = vortical part of transverse component of periodic unsteady velocity
$\hat{v}_i^+$ = i^{th} harmonic transverse gust
$|\hat{v}_i^+|$ = amplitude of the i^{th} harmonic transverse gust
W = periodic unsteady relative velocity from *NS* code
W_{NS} = periodic unsteady relative velocity from *NS* code
W_p = periodic unsteady relative velocity from potential code
$\bar{W}$ = time-mean relative velocity from *NS* code
$\bar{W}_{NS}$ = time-mean relative velocity from *NS* code
$\mathbf{x}$ = position vector
x/y = axial/circumferential coordinate
Z_g = axial gap (Fig. 9)
Z_s = axial coordinate downstream from stator trailing edge (Fig. 9)
Z_r = axial coordinate upstream from rotor leading edge (Fig. 9)
β_1 = inlet relative air angle
β_2 = exit relative air angle
Φ = flow coefficient
ϕ = velocity potential
ΔP = static pressure rise across compressor
ρ = density of fluid
κ = turbulence kinetic energy
Γ = circulation
ϵ = dissipation rate of turbulence kinetic energy
λ = normalized turbulence length scale
Ω = reduced frequency ($=\omega C/2\bar{W} = \pi s \cos \beta_1/\Phi$)
ω = rotor blade wheel angular frequency

Subscripts

∞ = inlet condition
b = blade
g = axial gap
i = harmonic number
NS = Navier–Stokes calculation
p = potential disturbance
r = rotor
s = stator
t = turbulence
v = vortical disturbance

Superscripts

$+$ = periodic unsteadiness or wall variable

$\rho C_\mu f_\mu (k^2/\epsilon)$, the turbulence Reynolds number $R_t \equiv (\rho k^2/\mu\epsilon)$, the wall variable $y^+ \equiv (\rho y U_\tau/\mu)$, and the wall shear velocity $U_\tau \equiv \sqrt{\tau_w/\rho}$.

3.1 Computational Domain and Discretization of Governing Equations. The computational domain is bounded by various boundaries as shown in Fig. 1. In this paper, each blade row is associated with a body-fitted embedded H-type grid. The GRAPE code (Sorenson, 1980) constitutes the majority of grid generation. For the isolated stator calculation, cells of 196 × 78 is used. For the stator/rotor configuration, 160 × 78, 172 × 78 and 184 × 78 cells per row is used for axial gaps of 10, 20, and 30 percent chord, respectively. The blade surface discretization contains 108 cells per blade surface. The resolution in time is 200 steps per blade-to-blade period.

Equations (1) to (4) are discretized and solved by SIMPLEC on a nonstaggered grid (Miller and Schmidt, 1988). We use the Crank–Nicolson scheme for time discretization, QUICK scheme (Leonard, 1979) for the convection term in momentum equations, and the first-order upwind scheme for $k-\epsilon$ equations. To avoid "checkerboard oscillation" of the pressure on nonstaggered grids, the pressure-weighted interpolation method (PWIM) of Miller and Schmidt is used to evaluate mass fluxes on control volume faces. This renders the converged solution independent of the underrelaxation factor.

3.2 Initial and Boundary Conditions. Various boundary conditions are specified as follows. The initial condition is a uniform flow imposed on impulsively started compressor blade rows with all flow variables having free-stream values. At the inflow boundary, which is 1.5 chord upstream of the stator leading edge, the potential influence of the stator row can be neglected, so it is reasonable to assume a uniform flow there. The turbulence kinetic energy and dissipation rate are specified through turbulence intensity Tu and its length scale λ nondimensionalized by the blade pitch, with Tu = 4 percent and λ = 0.003 corresponding to $R_t = 25$. At the outflow boundary, which is also 1.5 chord axially downstream of the rotor trailing edge, simple extrapolation boundary conditions, which assume that the flow does not evolve further in the axial direction, are imposed for all variables. On the blade surface, the no-slip condition is imposed. To avoid using very fine grids, the wall function approach is used to evaluate the wall shear stress τ_w.

The boundary treatment at the interface between two relatively moving grids is elucidated in Fig. 2, which shows an enlarged view of an instantaneous grid system near the interface. At this instant, the boundary value at the node P of the moving grid is found by interpolating the values at the solid-circle nodes of the stationary grid, which are known from the last iteration of the stator calculation. Linear interpolation is used for turbulence variables k, ϵ, μ_t, and cubic spline interpolation for all other variables. To reduce the error due to grid line skewness, Cartesian mesh is used near the interface. To ensure global mass continuity, the mass flux across the rotor grid boundary $\overline{AC}$ must equal to the sum of that across the stator grid boundaries $\overline{AB}$ and $\overline{BC}$. On periodic boundaries, direct periodic conditions are imposed for all variables. For the pressure and pressure correction, their normal derivatives vanish on the blade surface, or inflow/outflow boundaries.

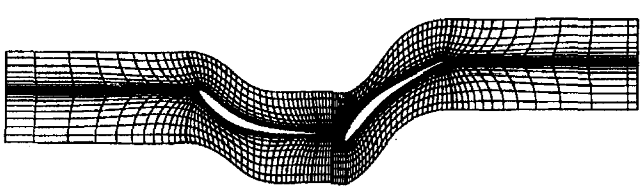

Fig. 1 The typical grid system for stator/rotor Navier–Stokes calculations (¼ grid density is shown for clarity)

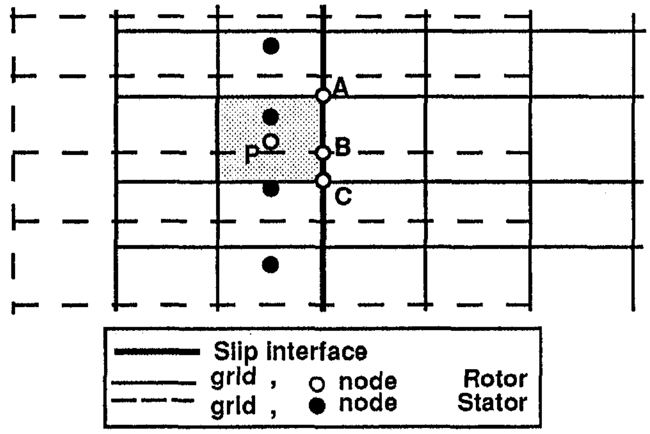

Fig. 2 Schematic showing data transfer between stator grid and rotor grid

3.3 Convergence Criteria. To determine convergence at the current iteration, the sum of the absolute residual of each finite difference equation for each variable is calculated. Convergence is reached when this sum is below 1 percent of that at the first iteration for all variables. For problems periodic in time, the whole flow field will approach a periodic steady state, after which the time-mean values are calculated for one further cycle. Such a state is defined by the smallest number of cycles, $n_{\rm cycle}$, so that the following convergence criterion is satisfied:

$$\frac{\dfrac{1}{N_{CV}} \displaystyle\sum_{i_{CV}}^{N_{CV}} |u_{i_{CV}}^{n_{\rm cycle}} - u_{i_{CV}}^{n_{\rm cycle}-1}|}{\displaystyle\operatorname*{Max}_{i_{CV}}(u_{i_{CV}}^{n_{\rm cycle}}) - \operatorname*{Min}_{i_{CV}}(u_{i_{CV}}^{n_{\rm cycle}})} \leq 10^{-4}, \qquad (5)$$

where i_{cv} is the index for the control volume and N_{CV} is the total number of control volumes. Computation is performed in an inhouse Cray YMP/EL four-processor machine. Typical calculation for stator/rotor configuration requires 3×10^{-4} CPU second per iteration per cell, with approximately 10 iterations per time step. About 20 to 30 blade to blade periods is required from impulsive start to periodic steady state. Thus, the total computational time is about 120 CPU hours.

4.0 Potential Calculation

For incompressible irrotational flow, the governing equation is

$$\nabla^2\phi = 0 \qquad (6)$$

with boundary condition $(\partial\phi/\partial n) = \mathbf{u}_b \cdot \mathbf{n}$. The Kelvin's theorem also holds, i.e., $(D\Gamma/Dt) = 0$. The Kutta condition used is that the velocity at the trailing edge is finite. The pressure is found using the unsteady Bernoulli's equation.

4.1 Solution Procedure. The vortex panel method with linearly varying strength is distributed on each panel. Each blade is composed of 64 surface panels. The resolution in time is 50 steps per blade-to-blade period. The influence coefficient of each surface panel is obtained by ten-point Gauss–Legendre integration. The Kutta condition is implemented by enforcing zero vorticity strength at blade trailing edges. With the bound circulation defined to be positive clockwise on both stator and rotor, Kelvin's theorem is satisfied by shedding vortices at each instant near the stator trailing edge from the pressure surface if the bound circulation is decreasing and from the suction surface if increasing. For the rotor, vortices are shed from the suction surface for decreasing circulation and from the pressure surface for increasing circulation (Basu and Hancock, 1978).

5.0 Validations

To verify the Navier–Stokes and potential codes, four test cases are presented. Two are taken from well-accepted data of AGARD (1990) and two from UTRC data.

5.1 Cascade Calculations. First, data from the UTRC subsonic cascade (Hobbs et al., 1980), tested near design point are used to validate both the Navier–Stokes and potential calculations. The test condition is Re = 4.78×10^5 and M = 0.113, which is appropriate for validation of incompressible codes. For the Navier–Stokes calculation, a 164×88 embedded H-type grid with 216 grid points per blade is used. At the inlet, Tu = 2 percent and $\lambda = 0.003$ is prescribed as the input to numerical simulation. For potential calculation, 46 surface panels per blade are used, and note that in this steady calculation, the strength of bound vortices is determined such that there is no upwash far upstream.

Figure 3 shows the distribution of the static pressure coefficient on the blade surface. The computational result agrees well with data along the whole blade surface except for regions near the separation bubbles where laminar–turbulent transition occurs at this Reynolds number, which is not modeled in the present study. Nevertheless, the overall pressure distribution seemed to be not greatly affected by the details of transition, and our assumption that the flow field is fully turbulent applies.

5.2 UTRC Multistage Compressor. Data from the UTRC low-speed multistage compressor, test case E/CO-5 in AGARD (1990), are used for comparison with the present calculation. This case is to test the capability of treating unsteady terms and interfacial boundaries in the Navier–Stokes calculations. The experimental compressor geometry consists of an inlet guide vane (IGV) followed by two nearly identical stages. Although in the experiment the IGV has 50 blades, rotor 44 blades, and stator 44 blades, equal blade number for all rows is assumed, as in Gundy-Burlet et al. (1991). The test condition is Re $\approx 3 \times 10^5$, M $\le$ 0.2, Φ = 0.51 and Tu = 0.5 percent. At the inlet, λ = 0.001 is prescribed as the input of numerical simulation. A grid system of 105×48 cells is attached to each blade row with 68 grid points per blade surface. The resolution in time is 200 steps per blade to blade period.

Figure 4 shows the distribution of time mean pressure coefficient on the rotor and stator of the second stage. The overall agreement with data is good except near the leading edge region. This is mainly due to lack of accuracy of the Navier–Stokes code near the leading edge and partly due to lack of information about the leading edge radius used in the experiment.

5.3 Far Wake Velocity Profile. This case involves the far-wake velocity profile of a low-speed compressor NACA 65 cascade, test case E/CA-1 in AGARD (1990). This and the following case are used to compare the two turbulence models considered. The ability to calculate wake profiles accurately lies mainly in the quality of the turbulence model used. The result is shown in Fig. 5. It can be seen that the Launder–Sharma (LS) model (Morse, 1991) and the standard high-Re (HR) model (Launder and Spalding, 1974) are about equal in capturing the far wake profile. The LS model seems to calculate the wake width slightly better than the HR model. Both predict the wake deficit on about an equal basis; the LS model slightly undershoots and the HR model slightly overshoots.

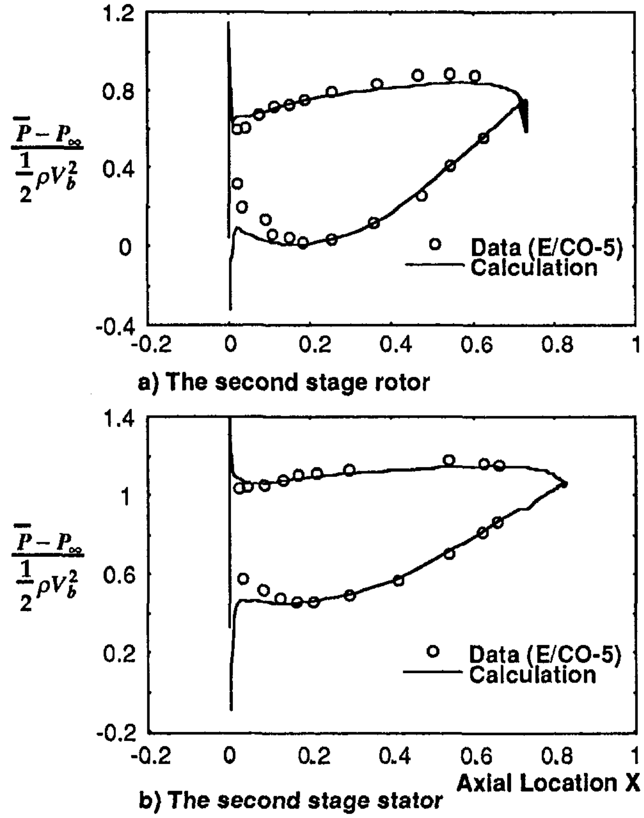

Fig. 4 Comparison between Navier–Stokes calculation and the second-stage time-mean surface pressure data on the UTRC low speed multistage compressor (test case E/CO-5 in AGARD, 1990)

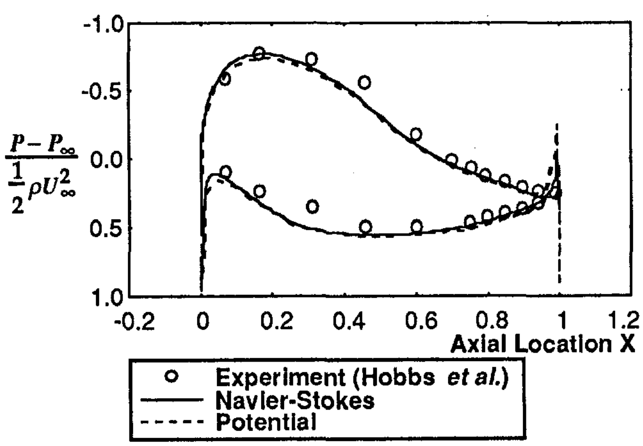

Fig. 3 Comparison between numerical results and surface pressure data on the UTRC low-speed cascade (Hobbs et al., 1980)

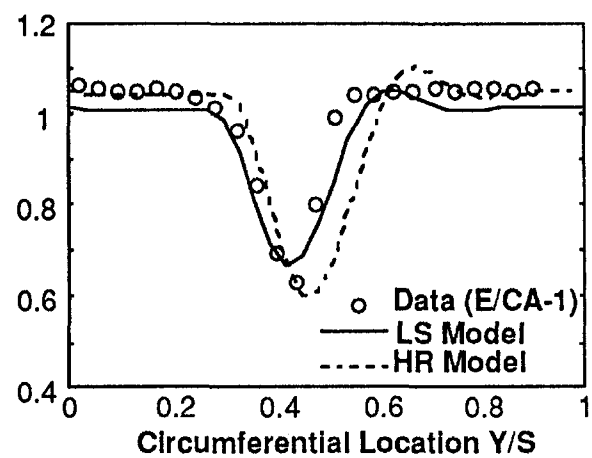

Fig. 5 Comparison between predictions by two turbulence models with data for the far wake total velocity at axial location 1.5 true chord aft of the blade leading edge at midspan (test case E/CA-1 in AGARD, 1990). Ve is the velocity at the midspan and midpitch location in the axial measuring plane used in the test case data.

5.4 Near-Wake Velocity Profile. The near-wake data, 0.1 chord downstream, in a single-rotor rig of UTRC (Dring, 1982), is also compared, as shown in Fig. 6. The LS model gives excellent prediction of the wake deficit but underpredicts the potential region. The HR model grossly overpredicts the deficit and does worse than the LS model on predicting the wake width. In light of calculations required for axial gaps of 10, 20, and 30 percent chord in this paper, the quality of the turbulence model in the near wake is more important than that in the far wake; thus the Launder–Sharma model is adopted.

6.0 Relationship Between Navier–Stokes and Potential Calculations

In this paper, both Navier–Stokes and potential codes are used to calculate vortical and potential disturbances; thus some comments are needed on the definition of the disturbances and the manner in which they are computed. The key approach taken here is that the potential disturbance, as defined below, calculated by the potential code, represents the potential disturbance included in the Navier–Stokes results, i.e.,

$$u_{NS}^{+} = u_{v}^{+} + u_{p}^{+} \tag{7}$$

$$v_{NS}^{+} = v_{v}^{+} + v_{p}^{+} \tag{8}$$

where u_{NS}^{+} and v_{NS}^{+} are streamwise and transverse gusts, respectively, from the Navier–Stokes code, u_p^+ and v_p^+ are potential disturbances from the potential code, and u_v^+ and v_v^+ are vortical disturbances from the difference between the Navier–Stokes and potential codes. Figure 7 illustrates this graphically. It is important to note that all disturbances are treated such that they are normal to and parallel with the local time-mean relative velocity vector, as computed by the Navier–Stokes code.

The manner in which the potential disturbances, u_p^+ and v_p^+, are extracted from the potential code do not include contributions from shed vortices. (Of course, in the calculation procedure vortices are shed as dictated by the Kelvin's theorem.) For a stator/rotor unsteady calculation, if the disturbance includes contributions from shed vortices, this potential disturbance would persist far downstream, which is not physical, since there is no mechanism for the shed vortices to decay. Thus, disturbances due to shed vortices are viewed as a viscous phenomenon due to the Kutta condition, and are included in the vortical disturbances, u_v^+ and v_v^+.

To justify our splitting procedure, the vortical and potential disturbances by Giles (see Appendix II of Manwaring and Wisler, 1993), which satisfy the splitting procedure of Goldstein (1978), are used to compare with the present calculated disturbances for flow downstream of the isolated stator. In Giles' formulation, disturbances from the rotor as seen in the stator frame are considered. For this paper, we consider disturbances from the stator as seen in the relative frame. Modifying Giles' formulation, the vortical disturbances in the relative frame are[1]

$$\tilde{u}_v = \bar{V}_z D e^{-iL(\theta - \bar{V}_\theta / \bar{V}_z z)} \tag{9}$$

$$\tilde{v}_v = \bar{V}_\theta D e^{-iL(\theta - \bar{V}_\theta / \bar{V}_z z)} \tag{10}$$

and the potential disturbances are

$$\tilde{u}_p = -LAe^{(-iL\theta - Lz)} \tag{11}$$

$$\tilde{v}_p = -iLAe^{(-iL\theta - Lz)} \tag{12}$$

Thus, their complex constants D and A in the relative frame are

$$D = \frac{i\hat{u} - \hat{v}}{i\bar{V}_z - \bar{V}_\theta} \tag{13}$$

$$A = -\frac{\bar{V}_z \hat{v} - \bar{V}_\theta \hat{u}}{L(i\bar{V}_z - \bar{V}_\theta)} . \tag{14}$$

Numerically, we computed Giles' formulation by first finding the values for D and A, from Eqs. (13) and (14), using results from the Navier–Stokes calculations. With D and A known, vortical and potential disturbances are found from Eqs. (9) to (12). The location $z = 0$ in Eqs. (9) to (14) is taken to be $Z_s/C = 0.058$ near design and 0.051 at high loading, since at these locations the two comparisons match for the transverse gust. (In the original analysis, the $z = 0$ point is arbitrarily taken to

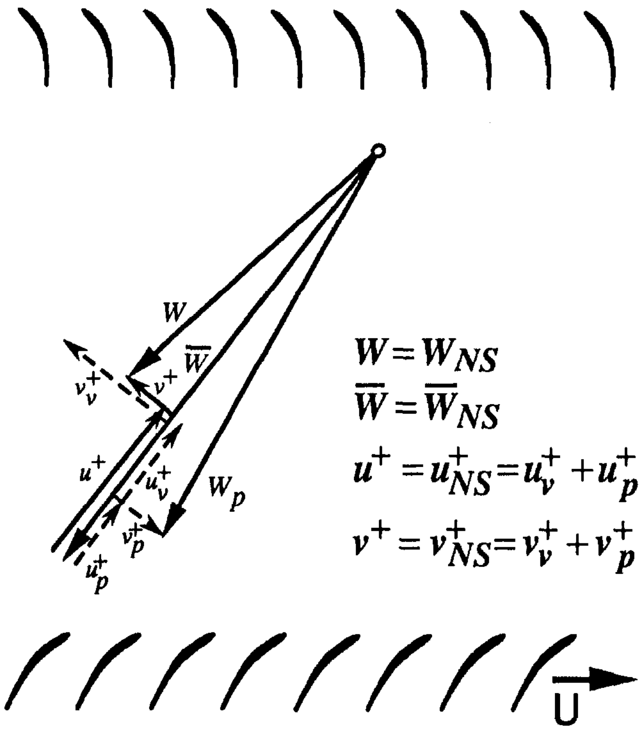

Fig. 7 Relative velocity vector diagram showing decomposition of vortical and potential disturbances from Navier–Stokes and potential code results (subscripts: *NS* = Navier–Stokes, *p* = potential, *v* = vortical)

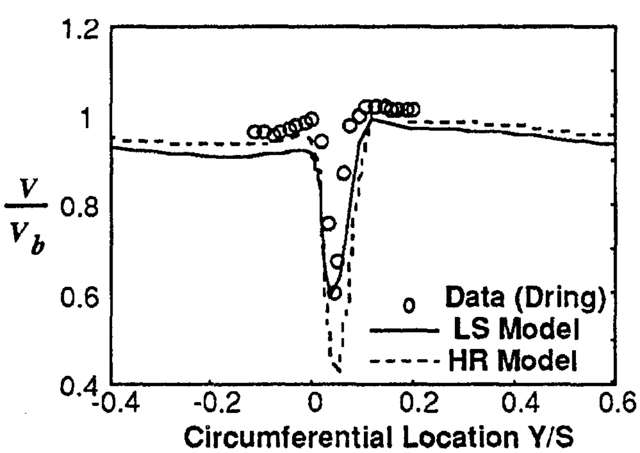

Fig. 6 Comparison between predictions by two turbulence models with data for the near-wake total velocity at axial location 0.1 axial chord aft of the blade trailing edge at midspan with Φ = 0.85 (Dring et al., 1982)

[1] Notations in Eqs. (9) to (14) are based on the original paper; u is the disturbance in the axial direction and v the disturbance in the tangential direction (the tilde and headed quantities represent the periodic unsteady and its first harmonic, respectively).

be the location of the hot wire.) Figure 8 shows the comparison between disturbances obtained from the present splitting procedure and those from Giles' formulation. Results show excellent agreement for the potential disturbances, which decay exponentially. The vortical disturbances do not agree as well since no viscous diffusion is considered in Eqs. (9) and (10), thus do not decay downstream. The flow physics will be discussed in more detail in Sec. 10.0. In summary, the present splitting procedure using results from the Navier–Stokes and potential codes to extract vortical and potential disturbances is believed to be physically sound.

7.0 Axial Coordinates

Two axial coordinates are used in this paper—one with the origin at the stator trailing edge extending aft, Z_s, and the other with the origin at the rotor leading edge extending forward, Z_r. Figure 9 provides a sketch of Z_s and Z_r. An example using stator/rotor configuration should help to clarify the need for the two axial coordinates when the axial gap varies. Consider Point A located 5 percent C axially upstream of the rotor leading edge for a gap, Z_g, of 30 percent C; then Point A is located at Z_s = 25 percent C and Z_r = 5 percent C. If the gap is reduced to 20 percent C with the Point A relative to the rotor held stationary, then the Point A is located at Z_s = 15 percent C and Z_r remains at 5 percent C. Thus, the coordinate Z_r is useful for describing flow variables, e.g., gusts, at locations held fixed with the rotor when the axial spacing varies, which is the case in this paper. From this example, the two coordinates are related by

$$Z_s = Z_g - Z_r \tag{15}$$

where Z_g is the axial gap. Also shown in the enlarged view in Fig. 9 is the location where the normalization of computed disturbances for stator/rotor interaction is taken, which will be described below.

8.0 Normalization of Disturbances

Normalization of vortical and potential disturbances is chosen such that the level of disturbances relative to the rotor for all axial gaps and loadings can be compared on an equal basis. For stator/rotor calculations, the Navier–Stokes calculated time-mean relative velocity, $\bar{W}$, at the location Z_r/C = 7.5 percent axially upstream of the rotor leading edge along the extension of the camber line is used to normalize gusts from both the Navier–Stokes and potential calculations (see Fig. 9). The location Z_r/C = 7.5 percent is chosed for two reasons: the coordinate Z_r is used, over other choices, since Z_r represents a fixed distance from the rotor for all axial gap cases, and the value of 7.5 percent is mainly due to the constraint imposed by the 10 percent gap case; this leaves only 2.5 percent chord from the stator trailing edge. The justification for using the Navier–Stokes calculated $\bar{W}$ to normalize the potential disturbance is based on the previously stated view that potential calculated gust represents potential disturbance in the Navier–Stokes calculation, Eqs. (7) and (8).

For the stator alone calculation, the Navier–Stokes calculated velocity at the exit plane as seen in the relative frame is used for normalization of disturbances.

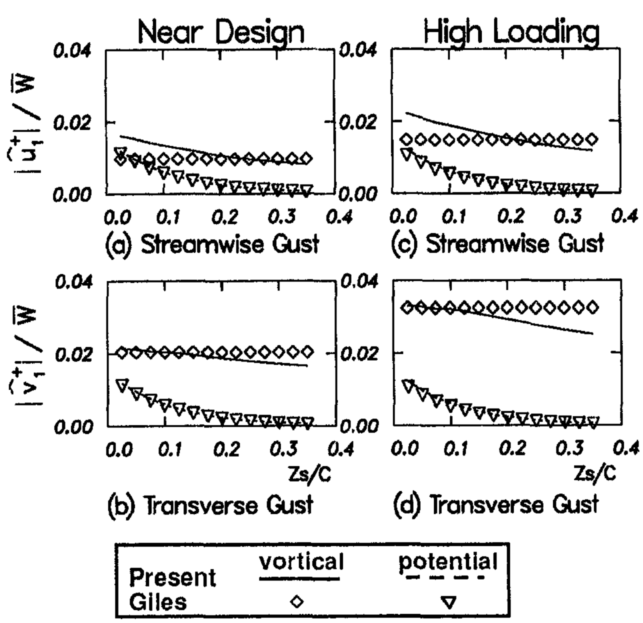

Fig. 8 Comparison of the present vortical and potential disturbance splitting procedure with that of Giles (Manwaring and Wisler, 1993)

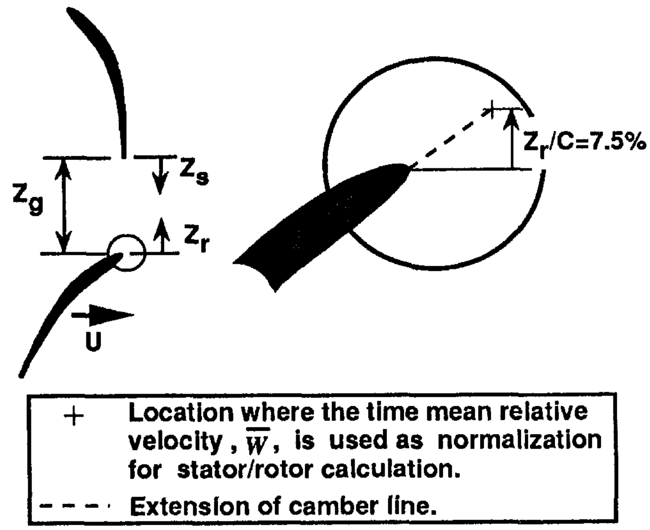

Fig. 9 Sketch showing the relationship between axial gap Zg and spatial coordinates Zs and Zr, $Zs = Zg - Zr$, and the location for normalization.

9.0 Blade Geometries and Stage Characteristics

Table 1 summarizes major blade geometries and flow parameters. The blades are that of a low-speed three repeating stage

Table 1 Blade geometry and flow conditions. The stator exit and the rotor inlet denote the axial location midway between the stator trailing edge and the rotor leading edge for the Zg/C = 30 percent case.

	Stator	Rotor
Camber	48.00°	35.00°
Stagger	20.67°	-39.50°
Solidity	1.415	1.415
Inlet relative angle, β_1, near design ($\Phi = 0.6$)	45.96°	56.80°
Exit relative angle, β_2, near design ($\Phi = 0.6$)	7.90°	32.34°
Inlet relative angle, β_1, at high loading ($\Phi = 0.5$)	53.55°	61.58°
Exit relative angle, β_2, at high loading ($\Phi = 0.5$)	8.64°	32.87°
Reduced frequency, Ω, near design ($\Phi = 0.6$)	----	4.057
Reduced frequency, Ω, at high loading ($\Phi = 0.5$)	----	4.231

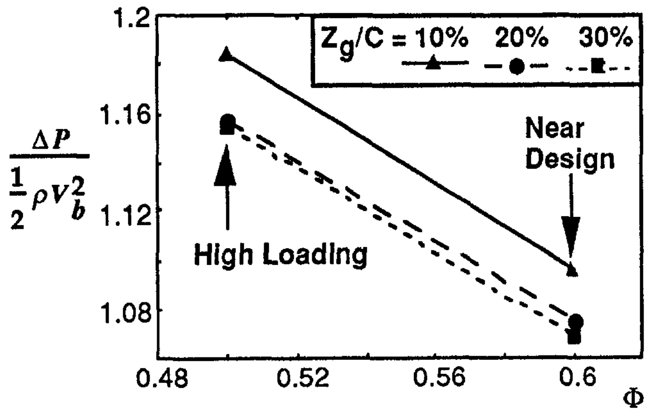

Fig. 10 Stage pressure rise characteristic for three axial spacings computed from Navier–Stokes calculations

axial compressor under construction. The Reynolds number, based on the inlet axial velocity, used in the computations is 1.59×10^5, corresponding to flow coefficient 0.6. The blades are designed using the controlled diffusion concept of Hobbs and Weingold (1984). As can be seen from a reduced scale sketch of Fig. 9, maximum flow diffusion is allowed near the minimum pressure region on the suction surface. Farther downstream, the blade surface is essentially a straight line extending to the trailing edge. The trailing edge thickness is 2 percent chord for both the stator and rotor.

The stage pressure rise characteristic computed by the Navier–Stokes code is shown in Fig. 10 for three axial gaps. It is clearly seen that pressure rise increases as the gap becomes smaller. At the near design point, the pressure rise for the 10 percent gap case is 2.5 percent higher than that of 30 percent case. This increase is consistent with the findings of Smith (1969) and Mikolajczak (1976).

10.0 Stator Alone Calculations

Since the rotor response is due to the forcing function from the stator, it is helpful first to define disturbances due to the stator without the presence of the rotor, as seen in the moving frame. As will be discussed, vortical and potential disturbances from the isolated stator calculation will be compared with those from stator/rotor calculation at the corresponding locations in the gap region. Thus, the degree to which disturbances are distorted due to the downstream rotor can be evaluated. Hence, results presented in this section are calculated with only the stator cascade. This is also conceptually equivalent to infinite axial gap between rows.

The modal amplitudes[2] of vortical and potential disturbances are presented in Fig. 11 for three distances behind the stator trailing edge, Z_s/C = 2.5, 12.5, and 22.5 percent. These three values correspond to a constant 7.5 percent chord axially upstream of the rotor leading edge, if the rotor is present, for gaps of Z_g/C = 10, 20, and 30 percent, respectively. Results show that, first, the vortical disturbance varies with loading but the potential disturbance essentially does not. The increase in vortical disturbance with loading should be related to the increase in the wake momentum thickness, thus leading to an increase in wake width. Results also suggest that the transverse component is larger than the streamwise gust. Since two-dimensional calculations are performed, any increase in vortical disturbance due to three-dimensional effects is not considered. Second, vortical disturbances are all greater than potential disturbances for all cases studied. This fact along with the slow axial decay characteristic of the vortical disturbance (see Fig. 12) suggests that the vortical disturbance plays a larger role in determining the rotor gust response than does the nonnegligible potential disturbance. Third, the vortical disturbance decays nearly linearly with increasing mode, except for mode 1 and 2 at Z_s/C = 2.5 percent, which is very close to the stator trailing edge.

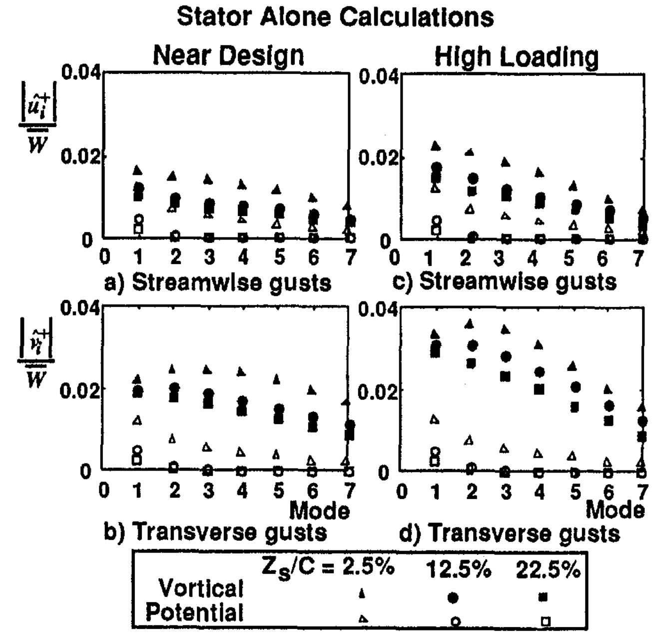

Fig. 11 Modal gust amplitudes as seen in the moving frame at three axial distances (Zs/C = 2.5, 12.5, 22.5 percent) behind the stator trailing edge. Calculations were done with stator alone.

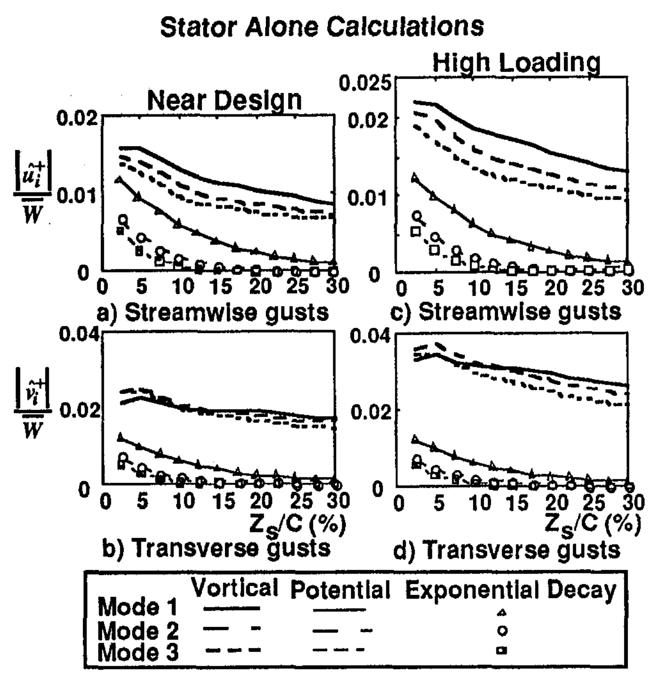

Fig. 12 Axial variation of modal gust amplitudes behind the stator trailing edge. Calculations were done with the stator alone with amplitudes as seen in the moving frame.

[2] The time domain output of both the Navier–Stokes and potential calculations are converted to a series of integer multiples of the rotor blade passing frequency using the standard Fast Fourier Transform (FFT), that is, the k^{th} point in the time domain can be written as

$$h_k = \sum_{n=0}^{N-1} H_n e^{-2\pi ikn/N}, \quad k = 1, 2, \ldots, N$$

The amplitude of the n^{th} mode is defined as H_n.

This suggests that several lower-order modes are important for determining the rotor gust response.

The axial variations of vortical and potential disturbances for the first three modes in both the streamwise and transverse directions as seen in the moving frame are presented in Fig. 12. First, the axial decay of vortical disturbance, unlike the potential disturbance, does not vary much with mode for the two loading levels. This again suggests that lower order modes are all important for determining the rotor gust response. Second, at 30 percent chord downstream of the isolated stator trailing edge, the potential disturbance is negligible compared to the vortical disturbance. However, at 10 percent chord, the transverse potential disturbance is about 1/3 that of vortical near design and 1/4 that at high loading. Thus, both disturbances must be considered for small axial gaps. Third, to show that the potential disturbance indeed follows an exponential axial decay, the analytical solution to the Laplace equation for potential flow is also plotted. For the ith mode, the transverse gust component is

$$\frac{\hat{v}_i^+}{W} = \left.\frac{\hat{v}_i^+}{W}\right|_0 \exp\left(-\frac{2\pi i}{S/C}\frac{Z_s}{C}\right), \qquad (16)$$

where the coefficient is the gust at $Z_s/C = 2.5$ percent. An identical exponential form applies for the streamwise gust, with a different value for the coefficient. The results, as plotted in Fig. 12, show that the potential disturbance calculated by the potential code (lines) agrees excellently with the analytical solution (symbols). Thus, the potential disturbance indeed decays exponentially with increasing modes, as opposed to vortical disturbance.

11.0 Stator/Rotor Calculations

Calculations for the stator/rotor configuration with axial gaps Z_g/C = 10, 20, and 30 percent using both Navier–Stokes and potential codes were performed. The focus was on the effect of the axial gap on the vortical and potential disturbances.

Figure 13 presents the vortical and potential disturbance amplitude for the stator/rotor calculation computed at three locations upstream of the rotor leading edge, Z_r/C = 2.5, 5.0, and 7.5 percent. Note that the results are plotted with the abscissa

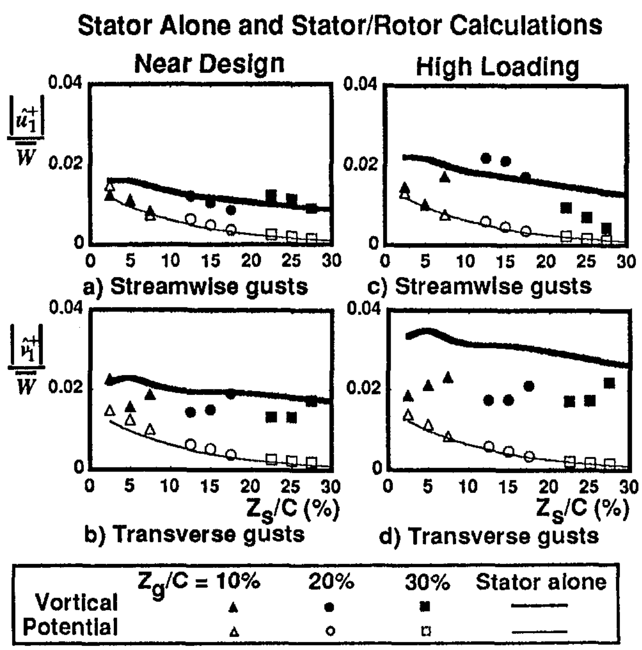

Fig. 13 Comparison of vortical and potential disturbances for the variable axial gap stator/rotor configuration with disturbances due to the stator alone

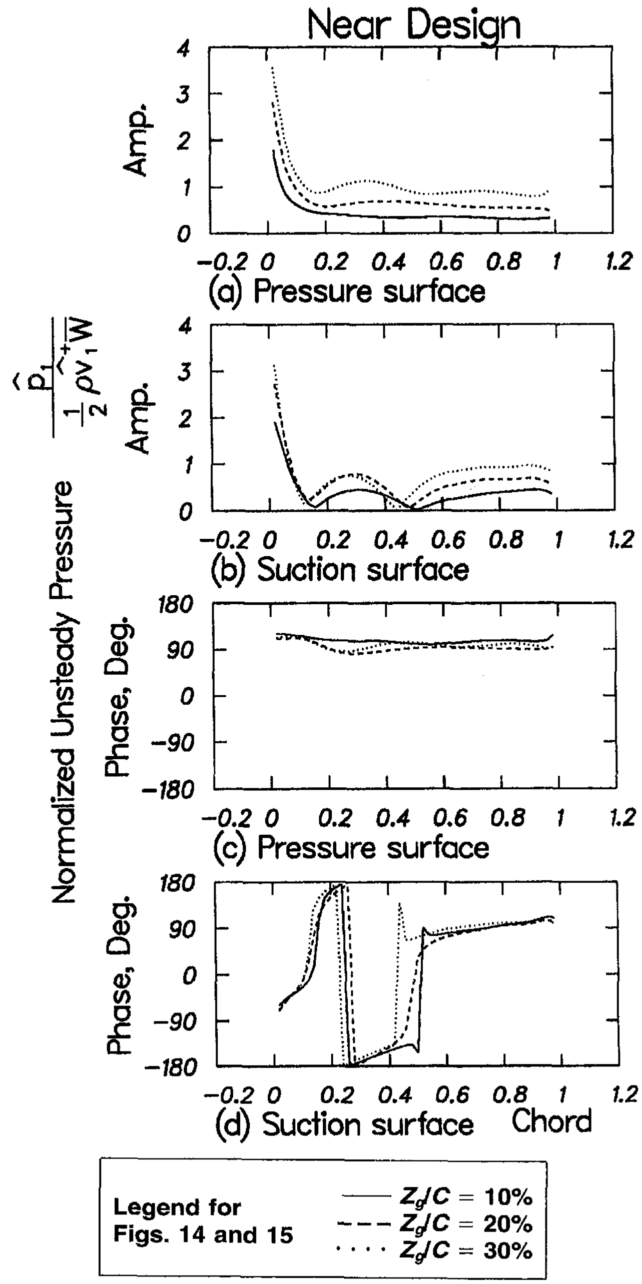

Fig. 14 Rotor surface pressure amplitude and phase (mode 1) for three axial gaps near design loading

extending from the stator trailing edge (see Fig. 9). Also shown are disturbances for the isolated stator calculation of Fig. 12. The comparison of potential disturbance between the stator alone calculation and the stator/rotor calculation shows that both streamwise and transverse potential disturbances are in good agreement for both loadings. This is perhaps a surprising result, which indicates that the potential disturbance in the relative frame for the stator/rotor configuration can be approximated by that for the isolated stator at the corresponding location in the gap region. One implication of this result is that the potential disturbance due to the rotor is locally uncoupled from that due to the stator; thus the rotor potential field does not interact with the stator potential field under the linear approximation, as suggested by Giles (1994). The comparison of vortical disturbance between the stator/rotor and stator alone configurations is not good as expected, especially at high loading. This suggests that stator/rotor interaction plays an important role in altering the vortical disturbance. The uncoupling/cou-

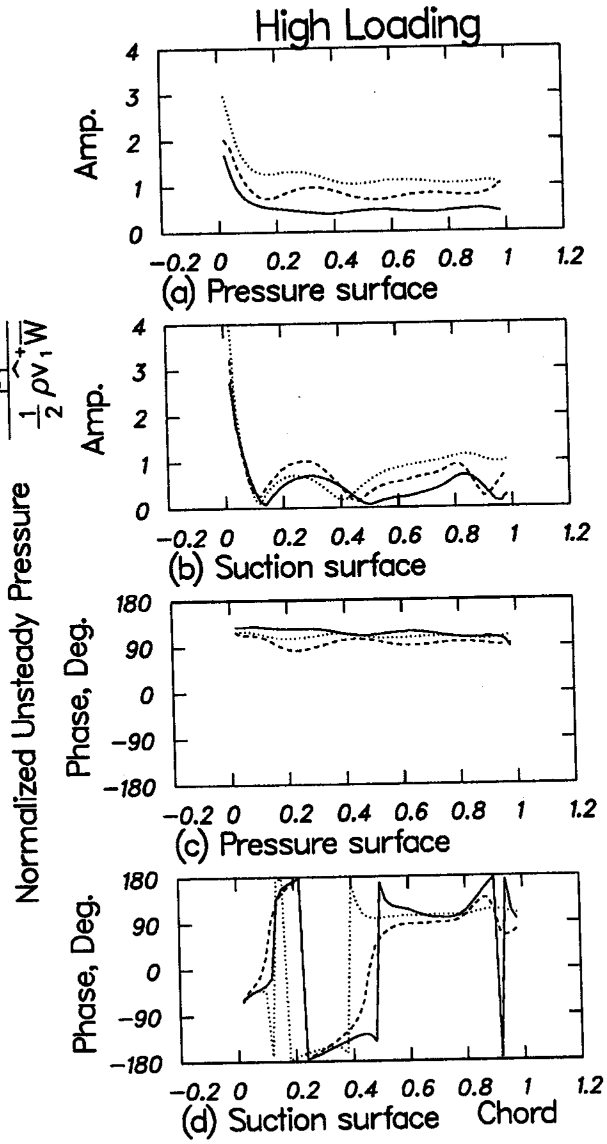

Fig. 15 Rotor surface pressure amplitude and phase (mode 1) for three axial gaps at high loading (see Fig. 14 for legend)

pling nature of the two disturbances is discussed further in Section 12.0.

The unsteady rotor surface pressure amplitude and phase for mode 1, computed by Navier–Stokes, are shown in Figs. 14 and 15, corresponding to near the design point and at high loading, respectively. Note that the normalization is based on the transverse gust, which includes both vortical and potential disturbances, and the time-mean relative velocity, both at Z_r/C = 7.5 percent upstream of the rotor (see Fig. 9). The normalized unsteady pressure on the pressure surface for both loadings, as seen in Figs. 14(*a*) and 15(*a*), appears to increase slightly as the axial gap increases. This is somewhat surprising, since the pressure is already normalized by the transverse gust including both vortical and potential disturbances. The normalized unsteady pressure on the suction surface, as seen in Figs. 14(*b*) and 15(*b*), shows two zero amplitude locations, which vary from about 10 to 15 percent chord and 40 to 50 percent chord with axial gap. The shifting of the upstream region, 10 to 15 percent chord, is smaller than that of the downstream region. The variation of local amplitude with axial gap seems to evolve within these two regions. The phase signatures on the pressure surface for both loadings suggest that essentially constant phase excitation is experienced by the airfoil. On the other hand, the phase signature on the suction surface exhibits a mixture of large phase variation with chord in the forward portion of the airfoil and a region near constant phase aft. This phase variation is also shown to be axial spacing dependent.

12.0 Discussions

The result of Fig. 13 suggests that the potential disturbance is uncoupled at the location calculated. The uncoupling is only local in nature. Numerics for the entire gap region reveal that upstream influence effect near the rotor leading edge contributes to alter the potential disturbance to differ from that for the stator-alone configuration, with the greatest difference near the stator trailing edge at 10 percent gap.

The vortical disturbance is coupled, or dependent on the stator/rotor interaction as shown in Fig. 13, most likely due to contributions from vortices shed into the wake in response to changes in the stator bound circulation. This is inherently a flow interaction resulting from fixed and moving blade rows. The net vortical disturbance as seen in the moving frame is due to the sum of the time-mean and unsteady wake profiles in the stator frame. The time-mean wake profile is mainly due to an isolated stator row as seen in its own frame. (In this case, the wake profile is steady, in the sense that blade row interaction is absent.) This wake profile contributes to the vortical disturbance like an observer fixed to the moving frame sweeping pass the time-mean wake of the isolated stator. This contribution to the vortical disturbance depends on the loading, which is convincingly shown in Fig. 13. The other contribution to the vortical disturbance is due to unsteadiness in the wake profile, which is a direct consequence of stator/rotor interaction.

13.0 Conclusions

The effect of compressor blade row axial spacing on vortical and potential disturbances and gust response for the stator/rotor configuration near the design point and at high loadings has been studied numerically using two-dimensional Navier–Stokes and potential codes. Calculations for axial gaps of 10, 20, and 30 percent chord were performed. Computations for an isolated stator have also been executed, which, by comparison with stator/rotor calculated disturbances, help in evaluating the level of flow interaction due to the presence of the rotor. Results are summarized as follows:

- Vortical and potential disturbances can be extracted from Navier–Stokes and potential codes successfully using the present splitting procedure (see Fig. 7).
- The potential disturbance from the isolated stator configuration is a good approximation for the potential disturbance in the gap region for stator/rotor calculations at the location studied. This suggests that potential disturbances from stator and rotor are locally uncoupled (see Fig. 13).
- The potential disturbance decays exponentially downstream and with increasing mode but does not vary with loading (see Fig. 12).
- The vortical disturbance is coupled, with blade row interaction effects depending on the axial spacing and loadings (see Fig. 14).
- Low-order modes of vortical disturbance are of substantial magnitude and decay much more slowly than do those of potential disturbance downstream (see Figs. 11 and 12).
- Vortical disturbance decays linearly with increasing mode except very close to the stator trailing edge (see Fig. 11).

Acknowledgments

We thank Prof. M. B. Giles, Oxford University, for his insightful discussion on the analysis in Appendix II of Manwaring and Wisler (1993). The authors gratefully acknowledge funding by the National Science Council of the Republic of China (NSC 84-2212-E-002-007). Partial funding of the computing cost by the Institute of Applied Mechanics is also appreciated. The second author acknowledges the help of Jesus Christ throughout the course of this work.

References

AGARD, 1990, "Test cases for computation of internal flows in aero engine components," AGARD Propulsion and Energetics Panel, Working Group 18, AGARD-AR-275.

Basu, B. C., and Hancock, G. J., 1978, "The unsteady motion of a two-dimensional airfoil in incompressible inviscid flow," *Journal of Fluid Mechanics,* Vol. 87, pp. 159–178.

Caruthers, J. E., and Dalton, W. N., 1993, "Unsteady aerodynamic response of a cascade to nonuniform inflow," ASME JOURNAL OF TURBOMACHINERY, Vol. 115, pp. 76–84.

Dring, R. P., Joslyn, H. D., and Hardin, L. W., 1982, "An investigation of axial compressor rotor aerodynamics," ASME *Journal of Engineering for Power,* Vol. 104, pp. 84–96.

Fleeter, S., Jay, R. L., and Bennett, W. A., 1981, "Wake induced time-variant aerodynamics including rotor–stator axial spacing effects," ASME *Journal of Fluids Engineering,* Vol. 103, pp. 59–66.

Gallus, H. E., Grollius, H., and Lambertz, J., 1982, "The influence of blade number ratio and blade row spacing on axial-flow compressor stator blade dynamic load and stage sound pressure level," ASME *Journal of Engineering for Power,* Vol. 104, pp. 633–641.

Giles, M. B., 1994, private communication.

Goldstein, M. E., 1978, "Unsteady vortical and entropic distortions of potential flows round arbitrary obstacles," *Journal of Fluid Mechanics,* Vol. 89, part 3; pp. 433–468.

Gundy-Berlet, K. L., Rai, M. M., Stauter, R. C., and Dring, R. P., 1991, "Temporally and spatially resolved flow in a two-stage axial compressor: Part 2—Computational assessment," ASME JOURNAL OF TURBOMACHINERY, Vol. 113, pp. 227–232.

Hetherington, R., and Moritz, R. R., 1976, "The influence of unsteady flow phenomena on design and operation of aero engines," AGARD-CP-177.

Hobbs, D. E., Wagner, J. H., Dannenhoffer, J. F., and Dring, R. P., 1980, "Supercritical airfoil technology program, wake experiments and modeling for fore and aft-loaded compressor cascades," Final report FR-13514, Pratt & Whitney Aircraft Group, UTC.

Hobbs, D. E., and Weingold, H. D., 1984, "Development of controlled diffusion aerofoils for multistage compressor applications," ASME *Journal of Engineering for Gas Turbine and Power,* Vol. 106, pp. 271–278.

Kielb, R. E., and Chiang, H. D., 1992, "Recent Advancements in Turbomachinery Forced Response Analyses," AIAA Paper 92-0012.

Launder, B. E., and Spalding, D. B., 1974, "The numerical computation of turbulent flow," *Comp. Meth. in Appl. Mech. and Eng.,* Vol. 3, p. 269.

Leonard, B. P., 1979, "A stable and accurate convective modeling procedure based on quadratic upstream interpolation," *Comput. Methods Appl. Mech. Eng.,* Vol. 12, pp. 59–98.

Manwaring, S. R., and Wisler, D. C., 1993, "Unsteady aerodynamics and gust response in compressors and turbines," ASME JOURNAL OF TURBOMACHINERY, Vol. 115, pp. 724–740.

Mikolajczak, A. A., 1976, "The Practical Importance of Unsteady Flow," AGARD-CP-177.

Miller, T. F., and Schmidt, F. W., 1988, "Use of a pressure-weighted interpolation method for the solution of the incompressible Navier–Stokes equations on a nonstaggered grid system," *Numerical Heat Transfer,* Vol. 14, pp. 213–233.

Morse, A. P., 1991, "Application of a low Reynolds number turbulence model to high-speed rotating cavity flows," ASME JOURNAL OF TURBOMACHINERY, Vol. 113, pp. 98–105.

Patankar, S. V., and Spalding, D. B., 1972, "A calculation procedure for heat, mass and momentum transfer in three-dimensional parabolic flows," *Int. J. Heat Mass Transfer,* Vol. 15, p. 1787.

Smith, L. H., 1969, "Casing boundary layers in multistage compressors," *Proc. Symposium on Flow Research on Blading,* Brown Boveri & Co Ltd, Baden, Switzerland 1969. in: Dzung, L. S., ed., *Flow Research on Blading,* Elsevier Publishing Company, 1970.

Sorenson, R. L., 1980, "A computer program to generate two-dimensional grids about airfoils and other shapes by the use of Poisson's equation," NASA-TM-81198.

Verdon, J. M., 1993, "Review of Unsteady Aerodynamic Methods for Turbomachinery Aeroelastic and Aeroacoustic Applications," *AIAA Journal,* Vol. 31, pp. 235–250.